g-C3N4/Ag@AgCl with Z-scheme Heterojunction and Ag electron bridge for Enhanced Photocatalytic Degradation of Tetracycline Wastewater

Baiyan Zhang (1281570975@qq.com)
Third Hospital of Shanxi Medical University: Shanxi Bethune Hospital
Hongfen Zhang
Shanxi Medical University
Dan Ma
Third Hospital of Shanxi Medical University: Shanxi Bethune Hospital
Fangmiao Liang
Shanxi Medical University
Hongli Lan
Shanxi Medical University
Feifei Yan
Shanxi Medical University

Research Article

Keywords: Photocatalytic degradation, g-C₃N₄/Ag@AgCl, Z-scheme heterojunctions, Electron bridge, Surface plasmon resonance

Posted Date: July 6th, 2023

DOI: https://doi.org/10.21203/rs.3.rs-2925616/v1

Version of Record: A version of this preprint was published at Environmental Science and Pollution Research on October 13th, 2023. See the published version at https://doi.org/10.1007/s11356-023-30183-7.

g-C_3N_4/Ag@AgCl with Z-scheme Heterojunction and Ag electron bridge for Enhanced Photocatalytic Degradation of Tetracycline Wastewater

Baiyan Zhang[1,2]*, Hongfen Zhang[2], Dan Ma[1], Fangmiao Liang[2], Honli Lan[2], Feifei Yan[2]

Third Hospital of Shanxi Medical University, Shanxi Bethune Hospital, Shanxi Academy of Medical Sciences, Tongji Shanxi Hospital, Taiyuan, 030032, China
School of Pharmacy, Shanxi Medical University, Jinzhong 030619, Shanxi, China

ABSTRACT

Building Z-scheme heterojunctions with an electron bridge is a favored function for increasing photocatalytic activity. A facile approach for preparing g-C_3N_4/Ag@AgCl ternary heterojunctions by co-precipitation and photoreduction was established in this work. First, via co-precipitation, AgCl was modified on the surface of g-C_3N_4 to create a broad contact area between AgCl and g-C3N4. The AgCl is then reduced to Ag via an in-situ photoreduction technique, resulting in the formation of a ternary composite. The experimental results showed that when g-C_3N_4 modified 25% of the Ag@AgCl, that is, g-C_3N_4/Ag@AgCl-25 had the best photocatalytic performance, 94.9% of TC was degraded within 240 minutes, and the reaction rate to TC was 0.1214 min^{-1}, which was 4.49 times and 8.12 times higher than that of g-C_3N_4 and Ag/AgCl, respectively. The excellent photocatalytic performance of g-C_3N_4/Ag@AgCl is attributed to the LSPR effect of Ag NPs and O-doping g-C_3N_4, which broadens the absorbance performance of g-C_3N_4, the establishment of Z-type heterojunctions between AgCl NPs and g-C_3N_4 NSs and Ag NPs as an electron transport bridge accelerate the photogenerated electrons transfer between AgCl and g-C_3N_4.

KEYWORDS: Photocatalytic degradation; g-C_3N_4/Ag@AgCl; Z-scheme heterojunctions; Electron bridge; Surface plasmon resonance

---

*Corresponding authors.

E-mail addresses: 1281570975@qq.com

Introduction

The map of antibiotic pollution in China's rivers shows an average antibiotic concentration of 303 ng/L, and major rivers from north to south are mired in antibiotic pollution [1]. Not only in China, but also in the global water environment [2, 3] . However, at present, the treatment efficiency of antibiotics in sewage treatment plants is limited, resulting in a large amounts of antibiotics being released directly into the environment and have been detected in various environments, especially in aquatic ecological environments. Antibiotics in water will mainly produce selective pressure on the resistance of environmental microorganisms and selective survival of drug-resistant pathogenic bacteria, causing serious pollution to surface water and groundwater, and then drug resistance in human and aquatic organisms, resulting in "super resistant bacteria", which once again seriously threatens human health. How to scientifically and effectively remove antibiotic residues in water is the focus of domestic and foreign researchers[4-6].

Photocatalytic oxidation is an excellent environmental purification technique because the process requires only inexpensive semiconductor photocatalysts and light sources[7-9]. Photocatalytic oxidation has some advantages, such as simple operation, low cost, cleanliness, high degradation efficiency, good stability and no secondary pollution[10-12]. However, photocatalysts are now generally faced with the problem that sunlight cannot be fully utilized and photogenerated carriers are easily recombination[13-15]. Various semiconductor nanomaterial modification strategies are now being investigated, which includes cocatalyst modification for enhancing reaction kinetics[16-18], loading on substrates that have excellent charge carrier mobility to achieve efficient charge extraction[19], compounding with bandgap-matched semiconductors to form heterojunctions[20], and modifying metals or oxides with surface plasmon resonance effects on semiconductor surfaces [21, 22].

Because of its simple synthesis, flexible electronic band structure, outstanding physicochemical

stability, rich content, and environmental friendliness, graphitic phase carbon nitride (g-C_3N_4) has attracted broad interest as an efficient non-metallic polymerized semiconductor photocatalyst [23, 24]. However, the high recombination rate and low conductivity of photogenerated electrons-holes limit the practical application of intrinsic g-C_3N_4[25, 26]. Many methods are now being researched to improve the photocatalytic efficiency of g-C_3N_4.

Silver halide has outstanding photocatalytic efficiency in degrading pollutants and is considered a promising candidate material [27, 28]. Among them, silver chloride (AgCl) is widely used in photocatalytic degradation field since it is non-toxic and easy preparation. The band structures of AgCl (E_{CB}= -0.05 eV and E_{VB}= 3.19 eV) and g-C3N4 (E_{CB}= -1.12 eV and E_{VB}= 1.58 eV) make AgCl and g-C3N4 suitable for constructing direct Z scheme paths [27, 29, 30]. However, because AgCl is prone to photocorrosion under ultraviolet irradiation, that is, AgCl is reduced to Ag^0. Therefore, modifying Ag on the surface of AgCl can transfer photogenerated electrons in AgCl to Ag in time to achieve the purpose of inhibiting the photocorrosion of AgCl [29].

Here, a ternary composite g-C_3N_4/Ag@AgCl nanomaterials have been synthesized using a simple in situ co-precipitation process and a photoreduction method in order to significantly improve the photocatalytic performance of g-C_3N_4. In the initial stages, a simple co-precipitation process was used to deposit AgCl NPs on the surface of g-C_3N_4. The deposited AgCl is then reduced under light irradiation to form a ternary composite with Ag as the electron transport medium between g-C_3N_4 and AgCl and light absorber. The loading Ag@AgCl can significantly improve the visible photocatalytic degradation of TC by g-C_3N_4 in aqueous media. In particular, the effects of Ag@AgCl loading, analytical adsorption equilibrium time of g-C_3N_4/Ag@AgCl, and pH of TC aqueous solution on the photocatalytic degradation performance were evaluated, and the degradation mechanism of g-C_3N_4/Ag@AgCl was further studied.

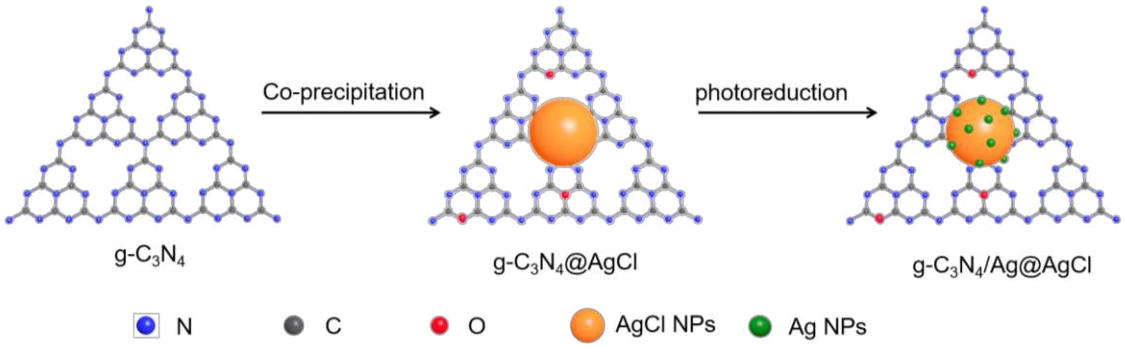

Scheme 1 Manufacturing procedure of g-C_3N_4/Ag@AgCl

2. Experimental

2.1 Synthesize of g-C_3N_4

All the reagents were of analytical grade and no further purification. g-C_3N_4 were prepared via thermal polymerization. 40 g of urea should be put in a porcelain crucible with a lid. It needs to be warmed in a Ksl-1100x muffle furnace at a rate of 10°C per minute from room temperature to 500°C, maintained warm for 4 hours, and subsequently allowed to cool naturally to room temperature. To create g-C3N4 powder, lumpy yellowish g-C3N4 was obtained and milled for 15 minutes.

2.2 Construction of g-C_3N_4/Ag@AgCl

In situ co-precipitation method and photoreduction method were used to construction g-C_3N_4/Ag@AgCl in Scheme 1. Depending on the loading levels, 30 mL of distilled water were utilized to dissolve 141.2 mg and 266.7 mg of $AgNO_3$ solids, and 0.8 g of g-C_3N_4 was fully dispersed in the $AgNO_3$ aqueous solution before being ultrasonically dispersed for 10 min. Excess 10% sodium chloride aqueous solution needs to be added dropwise and vigorously stirred for 10 hours in a dark atmosphere before the products are washed six times with distilled water and ethanol. For the formation of g-C_3N_4/Ag@AgCl-X, the prior obtained g-C_3N_4/AgCl-X was dispersed in 100 mL of distilled water, sonicated for a total of ten minutes, followed by being placed under a xenon lamp (>400 nm) for 30 minutes. The end product was then collected and dried in an oven at 50°C for a total of 10 hours. The sample prepared without the

g-C_3N_4 using the same preparation method is Ag@AgCl.To generate AgCl, an excess of 10% sodium chloride solution was slowly added to a silver nitrate solution dropwise while stirring vigorously. The resulting mixture was then stirred in dark conditions at ambient temperature for 10 hours. Ag@AgCl was obtained by dispersing the synthesized AgCl in 100 mL of purified water, sonicating it for 10 minutes, and then exposing it to xenon radiation (> 400 nm) for 30 minutes. The end product was then collected and dried in an oven at 50°C for 10 hours.

2.3 Characterization

Transmission electron microscopy (TEM) and high-resolution transmission electron microscopy (HRTEM) were measured on a JEOL-2100F microscope equipped with a 200 kV accelerating voltage to investigate both the microstructure and the morphology of the nanomaterials as-prepared. The DX2700B X-ray diffractometer, which has a scanning speed of 4°/min, a step size of 0.06, and a scanning range of 10°-80°, was used to capture the crystal structure of each component in the sample. The sample's surface content, chemical state, and elemental composition were all measured using an X-ray photoelectron spectrometer made by Thermo Scientific, model number ESCALAB 250Xi. Test conditions: The X-ray source is Al target Kα 1486.6 eV, and the binding energy of each element in the sample is calibrated with contaminated carbon C 1s 284.6 eV. XPS Peak 4.1 was used for fitting and peak splitting. The absorption range of light from the sample is tested by a UV-Vis absorption spectrum. Test conditions: Wavelength range 200-1000 nm, with barium sulfate as blank.

2.4. Photocatalytic degradation experiments

Under visible light irradiation, the samples' photocatalytic degradation activity in TC solution has been evaluated. After 30 minutes of stirring in a dark environment with the constructed nano-materials dispersed in TC solution, the adsorption-desorption equilibrium between the material and TC was

achieved. Then, at a height of 13 cm from the surface of the liquid level to the lamp, a 300 W xenon lamp (>400 nm) with a filter is illuminated from the reactor's top. The resulting suspension (3 mL) was taken out from the reactor at regular intervals and filtered using a 0.45 m aqueous filter head.

The absorbance of the filtrate was measured with a UV-1200 ultraviolet (UV) spectrophotometer at the maximum absorption wavelength of TC at 356 nm, and the degradation rate was obtained using the equation:

$$\eta=(C_0-C_t)/C_0\times100\%$$

$$=(A_0-A_t)/A_0\times100\%$$

$$Ln\left(\frac{C_0}{C_t}=\frac{A_0}{A_t}\right)=Kt$$

2.5 Photoelectrochemical measurement

A CHI660E electrochemical workstation (Shanghai ChenHua Instrument Co., Ltd.) equipped with a 300 W Xenon lamp (CEL-HXF200-T3, Beijing Zhongjiao Jinyuan Technology Co., Ltd.) is used to measure the photoelectrochemical characteristics (PEC) of nanomaterials. Standard three-electrode electrochemical analysis apparatus is used. The reference and counter electrodes utilized were Ag/AgCl and Pt wires, respectively. The working electrode is constructed with a series of nano-material modified conductive glass modified (FTO glass). In the electrochemical impedance test (EIS), the high-frequency region of the Nyquist diagram is controlled by the electrode reaction kinetics, so the impedance of nanomaterials can be tested by comparing the size of the semicircle radius in the high-frequency region. The frequency range of the EIS test is from 0.005 to 10^6 Hz with amplitude of 10 mV. The three electrodes was soaked in 30 mL PBS solution (pH 7.4) and 5 mM $[Fe(CN)_6]^{3-/4-}$. The photocurrent response can directly reflect the separation efficiency of photogenerated carriers in nanomaterials. In the identical three-electrode setup, photocurrents carried out. The three electrodes was measured in 30 mL PBS

solution (pH 7.4), irradiated with a 300 W xenon lamp.

3. Results and Discussion

3.1 Morphology and structure characterization of g-C_3N_4/Ag@AgCl-X

The morphological features of g-C_3N_4 and g-C_3N_4/Ag@AgCl-X are observed in Fig.1. The TEM of g-C_3N_4 and g-C_3N_4/Ag@AgCl-X indicated that g-C_3N_4 has a layered shape and an amorphous framework, as illustrated in Fig.1a-1b. In the TEM of g-C_3N_4/Ag@AgCl-X (Fig. 1c), with an average particle size of 4.76 nm, the Ag@AgCl NPs were evenly modified on the external layer of g-C_3N_4. HRTEM reveals visible lattice distance at 0.277 nm and 0.236 nm (Fig. 1d), which are nearly identical to the (200) plane of AgCl and the (111) plane of Ag[31].

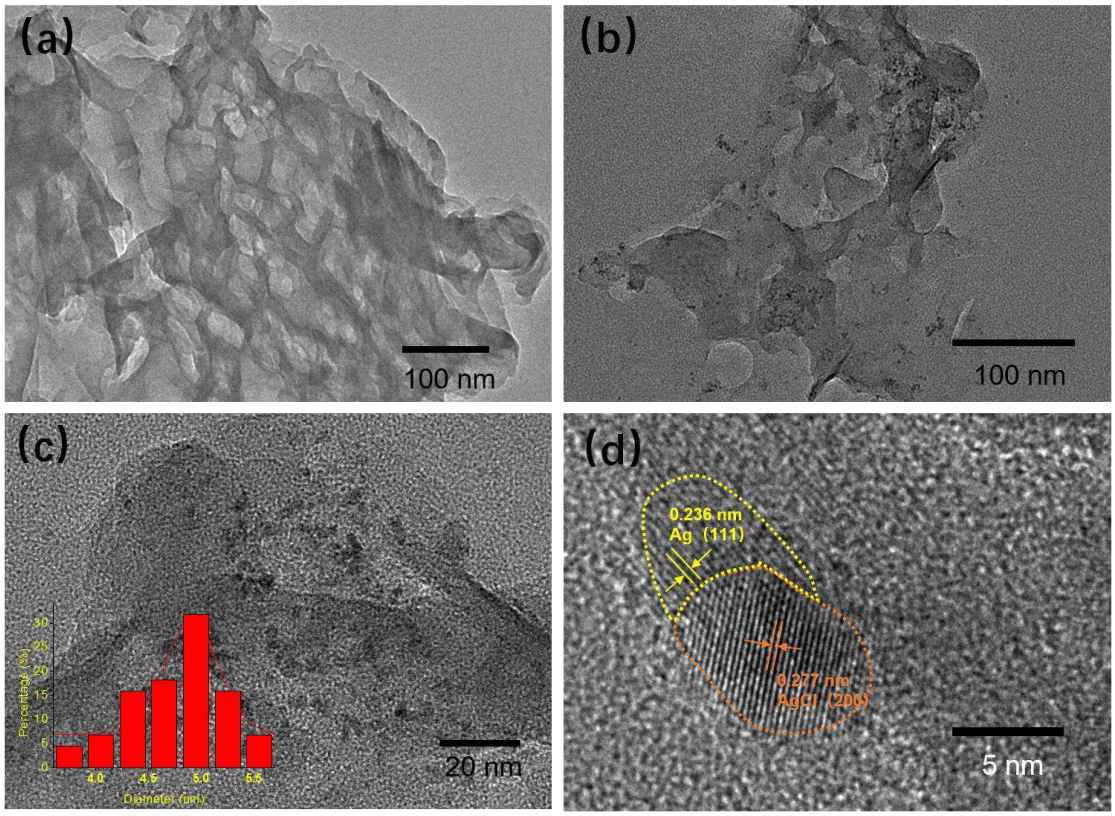

Fig.1 TEM of g-C_3N_4 (a), g-C_3N_4/Ag@AgCl-25 (b, c) and HRTEM of g-C_3N_4/Ag@AgCl-25

The crystalline form of g-C_3N_4/Ag@AgCl-X was studied by XRD. As exhibited in Figure 2a, diffraction peaks appeared at 27.8°, 32.6°, 46.5°, 55.2°, 57.8°, 67.9°, 74.7°, and 77.1°. The diffraction peak of 27.8° belongs to the (002) crystal plane of g-C_3N_4[32], which is the result of the

accumulation of conjugated aromatic systems. These diffraction peaks of 32.6°, 55.2°, 57.8°, 67.9°, 74.7°, and 77.1° belong to the (200), (311), (222), (400), (331), and (420) crystal planes of the AgCl cubic phase (JCPDS#06-0480) [33], respectively. In addition, the diffraction peak at 38.4° is weak, and a clear peak can be seen in the zoomed-in view of Figure 1b, which belongs to the (002) crystal plane of Ag. The aforementioned results show that we have successfully constructed a g-C_3N_4/Ag@AgCl ternary complex.

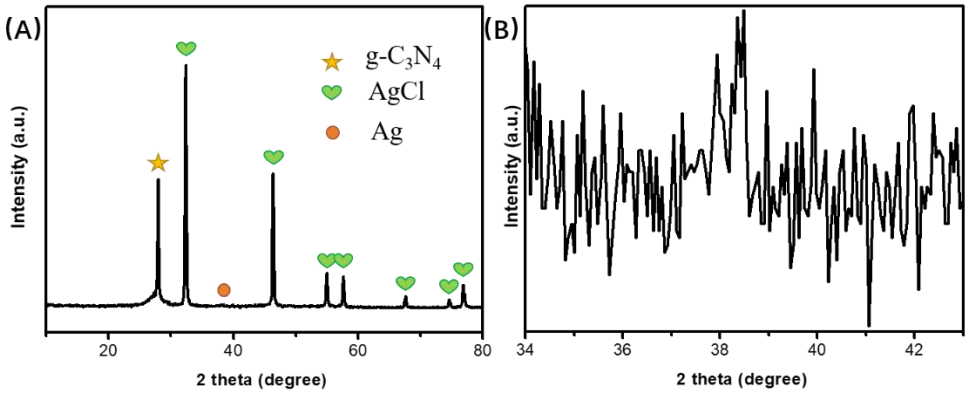

Fig.2 (a) XRD patterns of g-C3N4/Ag@AgCl-25 in the range of 20°-80°; (b) in the range of 34°-43°

XPS spectroscopy is applied to investigate the surface chemical state and the interactions between g-C_3N_4/Ag@AgCl-X and g-C_3N_4 materials, as shown in Figure 2. From the XPS full spectrum (Figure 2a), g-C_3N_4/Ag@AgCl-X contains peaks of Ag and Cl in addition to C, N, and O peaks compared with g-C_3N_4, indicating that the g-C_3N_4 surface is successfully loaded Ag@AgCl, which corresponds with the XRD results. In figure 2b, after depositing Ag and AgCl on the surface of g-C_3N_4 by ordinary chemical precipitation, the O content in g-C_3N_4/Ag@AgCl increases significantly, because the process of forming Ag and AgCl is carried out in an aqueous solution environment, so that O is doped into g-C_3N_4 in the form of O-H, C-O, C=O and O-C=O [34]. Three peaks for g-C_3N_4 at 397.7 eV, 399.6 eV, and 400.6 eV in the N1s spectra (Figure 2c) correspond to C-N=C, $N(C)_3$, and NH_X in the triazine ring structure, respectively. In contrast to C_3N_4, g-C_3N_4/Ag@AgCl exhibits a novel N-C=O functional group, demonstrating that part of the N in the compound has been replaced by O. This is in line with the rise in

O content depicted in Figure 2b. In addition, after the modification of Ag and AgCl, the peaks of C-N=C, $N(C)_3$ and NH_x transfer to higher binding energies. This is due to the fact that nitrogen groups that have large local electron densities in g-C3N4 can give solitary pairs of electrons to the vacants orbitals of Ag atoms, stabilizing Ag via metal support interactions and resulting in high dispersion of Ag and AgCl. In addition, the C1s spectra of g-C_3N_4/Ag@AgCl in Figure 2d contain three peaks of 284.8 eV, 286.1 eV and 288.3 eV that are attributable to N=C-N, C-O, and graphitic carbon in the triazine framework [35, 36]. C1s of g-C_3N_4/Ag@AgCl have a new C-O peak compared to C1s of g-C_3N_4, consistent with O1s results. Four peaks can be seen in the high-resolution XPS spectra of Ag3d, which is depicted in Figure 3e. The peaks at 367.3 eV and 373.3 eV are associated with Ag 3d5/2 (Ag^+) and Ag 3d3/2 (Ag^+), respectively. The two remaining peaks, assigned to Ag 3d5/2 (Ag^0) and Ag 3d3/2 (Ag^0), are situated at 374.1 eV and 368.1 eV, respectively. The Cl2p XPS peak can also be split into two characteristic peaks that are both associated with AgCl, at 197.6 eV and 199.3 eV, respectively[33]. The coexistence of Ag@AgCl and g-C_3N_4 in g-C_3N_4/Ag@AgCl composites is confirmed by all of these investigations.

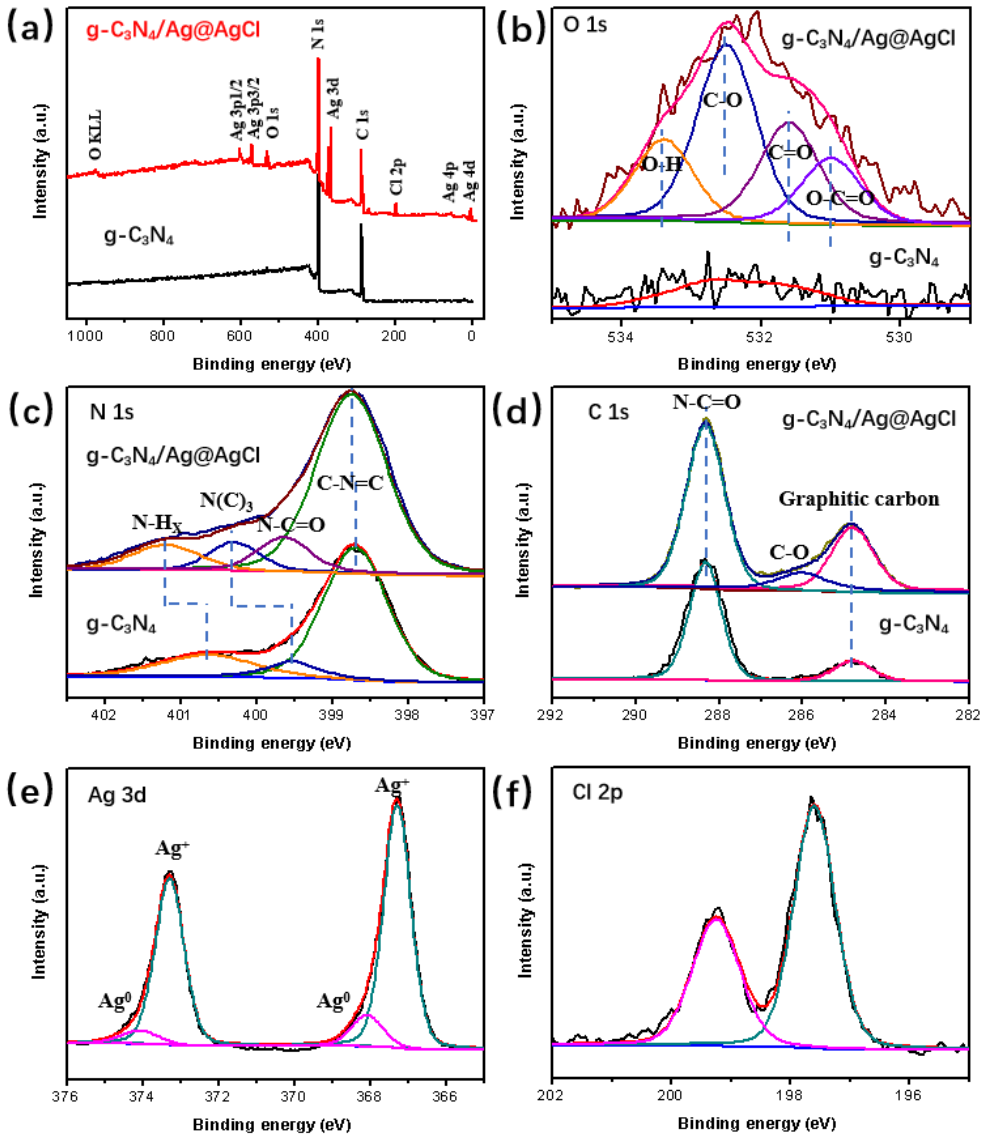

Fig.3 XPS survey spectra (a) and high-resolution XPS spectra of O 1 s (b), N 1 s (c), C 1 s (d), Ag 3d (e) and Cl 2p (f) for g-C_3N_4 and g-C_3N_4/Ag@AgCl-25

3.2 Absorbance and carrier separation characteristics

As we all know, metal modification and heterostructure between semiconductors are significant strategies for controlling the optical and electrical properties, which in turn impacts their photocatalytic efficacy. In Figure 4, the absorbance properties of g-C_3N_4, AgCl, Ag@AgCl, g-C_3N_4/AgCl, and g-C_3N_4/Ag@AgCl were evaluated by UV-vis diffuse reflectance spectra. Due to its absorption edge at

about 432 nm, g-C3N4 exhibits an 2.87 eV band gap. Due to its absorption edge at 419 nm, AgCl exhibits an 2.96 eV band gap. The surface plasmon resonance (SPR) effect of the Ag NPs on the surface of AgCl NPs by in situ photoreduction [38] and O-doped g-C3N4 [39] is responsible for the slight redshift of the absorption edge observed in g-C_3N_4/Ag@AgCl comparison with g-C3N4 and AgCl. Furthermore, the SPR effect of Ag nanoparticles may be used to explain the considerable improvement in the visible area in the absorption strength of g-C3N4/Ag@AgCl composites [21]. For the purpose of to achieve high photocatalytic performance, the integration of g-C3N4 with Ag@AgCl NPs may significantly enhance the visible light response and the utilization efficiency of solar energy.

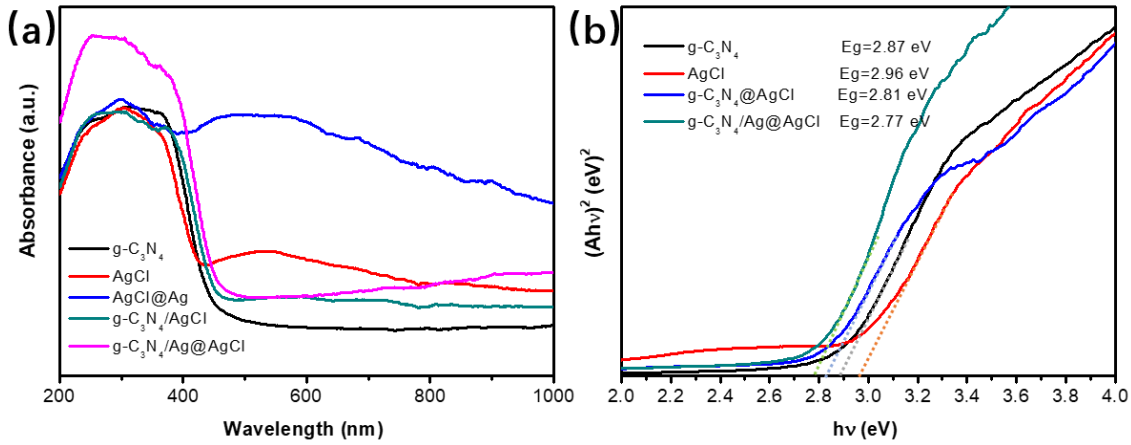

Fig.4 UV-vis absorption spectra (a), Tauc plots (b) of the prepared nano-materials

EIS and photocurrent responses were used to examine the charge separation and transfer capabilities of g-C_3N_4 and g-C_3N_4/Ag@AgCl. Figure 5a shows that g-C_3N_4/Ag@AgCl-25 shows significantly enhanced photocurrent density compared to g-C3N4 and g-C_3N_4/Ag@AgCl-15, further verifying that g-C_3N_4/Ag@AgCl-25 exhibits higher charge separation and transfer efficiency (Figure 5a). The sample's arc radius rose in the following order: g-C_3N_4; g-C_3N_4/Ag@AgCl-15; and g-C_3N_4/Ag@AgCl-25, revealing that this material has the lowest electrochemical impedance during the photocatalytic reaction. The results above imply that heterojunction formation between AgCl and g-C_3N_4, Ag SPR, Ag as an electron bridge, and O-doping in g-C_3N_4 are responsible for the improvement in carrier separation and transfer efficiency.

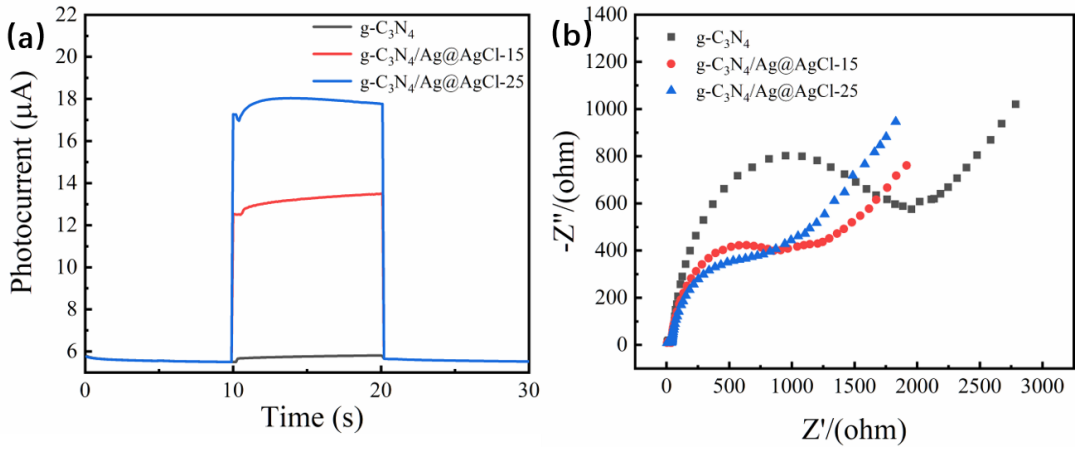

Fig. 5 EIS spectra (a) and photocurrent responses(b) of C_3N_4, g-C_3N_4/Ag@AgCl-15 and g-C_3N_4/Ag@AgCl-25.

3.3 Tetracycline photocatalytic degradation properties

The dosing quantity and desorption adsorption equilibrium time of g-C3N4/Ag@AgCl were tuned to increase the photocatalytic effectiveness, as demonstrated in the supporting information (Figure S2-S3).

A 300 W xenon lamp (wavelength greater than 400 nm) was used to photocatalyze the degradation of TC (30 mg L^{-1}) under visible light for 60 minutes using 20 mg of each of the following catalysts: AgCl, g-C3N4, Ag@AgCl, g-C_3N_4@AgCl, and g-C_3N_4/Ag@AgCl. The results are shown in Figures 7a and 7b. TC virtually does not self-degrade when exposed to visible light in figures S1. The order of each nanomaterial's photocatalytic performance was g-C_3N_4/Ag@AgCl > g-C_3N_4@AgCl > g-C_3N_4 > Ag@AgCl = AgCl. The adsorption performance of each material to TC is poor, so TC degradation is mainly a photocatalytic degradation process. It can be demonstrated from the significantly improved photocatalytic performance of g-C3N4@AgCl compared to g-C3N4 and AgCl that the creation of heterostructures between g-C3N4 and AgCl improved the separation efficiency of photogenerated electrons and holes. Ag@AgCl had similar degradation TC properties to AgCl, indicating that AgCl

played a major role in Ag@AgCl and AgCl, and the cocatalyst and SPR effect of Ag were negligible. g-C_3N_4/Ag@AgCl has the best photocatalytic performance, indicating that the heterogeneous structure between g-C_3N_4 and AgCl, the Ag as electron transport, and the SPR of Ag synergistic enhance its photocatalytic properties.

Further research was done on the impact of Ag@AgCl loading on the photocatalytic performance of g-C3N4/Ag@AgCl. Figure 7c demonstrates that as the amount of Ag@AgCl alteration increases, so does the photocatalytic performance. g-C_3N_4/Ag@AgCl-25 demonstrated improved photocatalytic performance, and the degradation efficiency of TC reached 85.2% in 60 min, which was 4.49 times and 8.12 times higher than that of g-C_3N_4 and Ag/AgCl, respectively. When combined with the structure and photoelectric characterization of g-C_3N_4/Ag@AgCl, the results show that the SPR effect of Ag NPs and O-doping broadens the absorbance performance of g-C_3N_4 and Ag NPs acts as an electron transport bridge to promote the transfer of photogenerated electrons between AgCl and g-C_3N_4.

The pH of the TC solution was adjusted using HNO_3 and NaOH solutions, respectively, and the influence of pH on degradation rate was explored. The results are presented in Figure 7d under the conditions of dark reaction for 20 min, catalyst dosage of 20 mg, and initial TC content of 20 mg L^{-1}. The pH of the TC degradation rate from high to low was 7.0, 3.0, and 11.0 after 30 minutes of reaction time. The degradation rate of TC under acidic and neutral circumstances for 30 minutes was nearly identical, reaching 80.78% and 80.91%, respectively, but it was only 73.34% under alkaline conditions. This result indicates that TC can be well degraded under both acidic and neutral conditions. In addition, the initial concentration of TC is examined in Figure S4, which indicating g-C_3N_4/Ag@AgCl-25 efficiently degrades TC solutions from 10 mg□L^{-1} to 30 mg□L^{-1}.

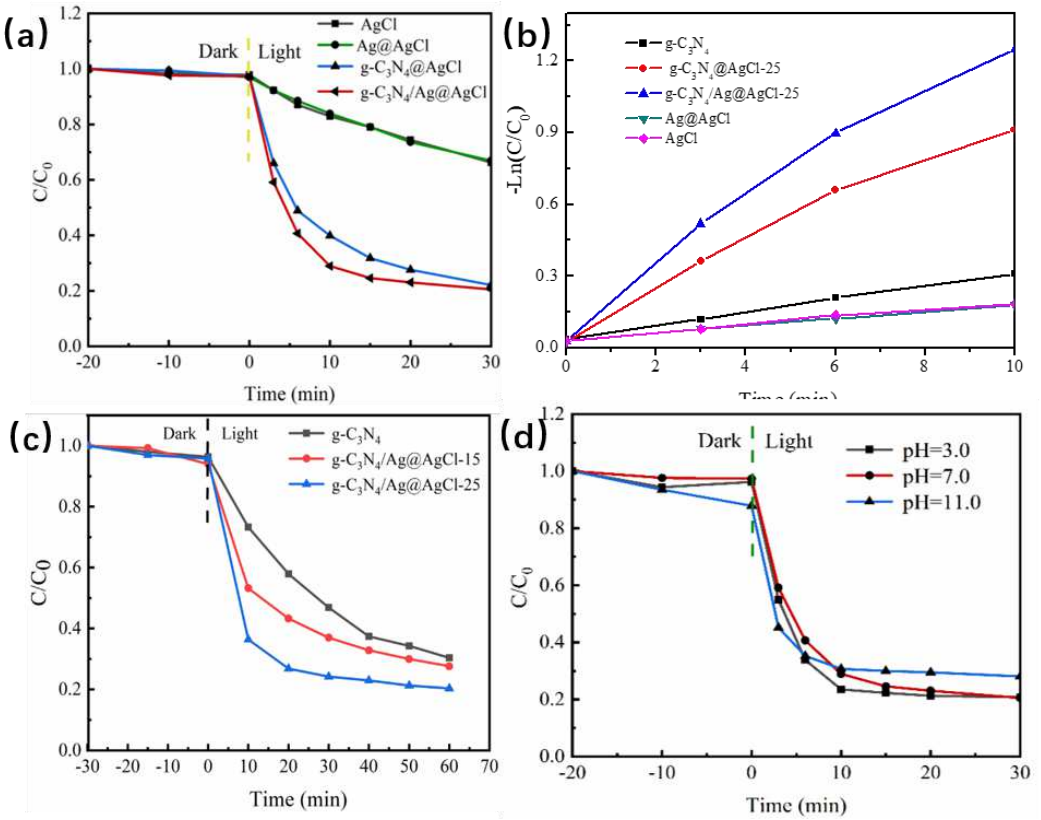

Fig. 6 TC photocatalytic performance (a, c, d) and ratios (b) of the prepared nano-materials

3.4 Photocatalytic degradation mechanism

Photogenerated electrons (e-) and holes (h+) on the photocatalyst surface engage in the degradation reaction under visible light circumstances, producing various photocatalytic degradation pathways. Ascorbic acid (AA), EDTA-2Na, isopropanol (IPA), and AgNO3 were used to capture superoxide radicals (·O_2^-), h^+, hydroxyl radicals (·OH), and electrons (e^-) in order to explore the photocatalytic mechanism of the g-C_3N_4/Ag@AgCl-25 photocatalyst on TC under visible light conditions [40, 41]. The photocatalytic degradation rates of g-C_3N_4/Ag@AgCl-25, as shown in Figure 8, were 18.35% and 13.41%, respectively, with the addition of AA and EDTA-2Na, revealing that ·O_2^- and h^+ were the main active species in the degradation process and the h^+ effect was stronger than that of ·O_2^-. Interestingly, when $AgNO_3$ is used as an electron trapper, the degradation efficiency of TC is slightly improved, because after $AgNO_3$ captures electrons, it facilitates the separation of electrons and holes, so that more

holes are used to degrade TC. In addition, the addition of IPA has almost no effect on g-C_3N_4/Ag@AgCl-25 degradation TC. In summary, $\bullet O_2^-$ and h^+ are the main active species in the degradation of TC by g-C_3N_4/Ag@AgCl-25 photocatalysts under visible light conditions.

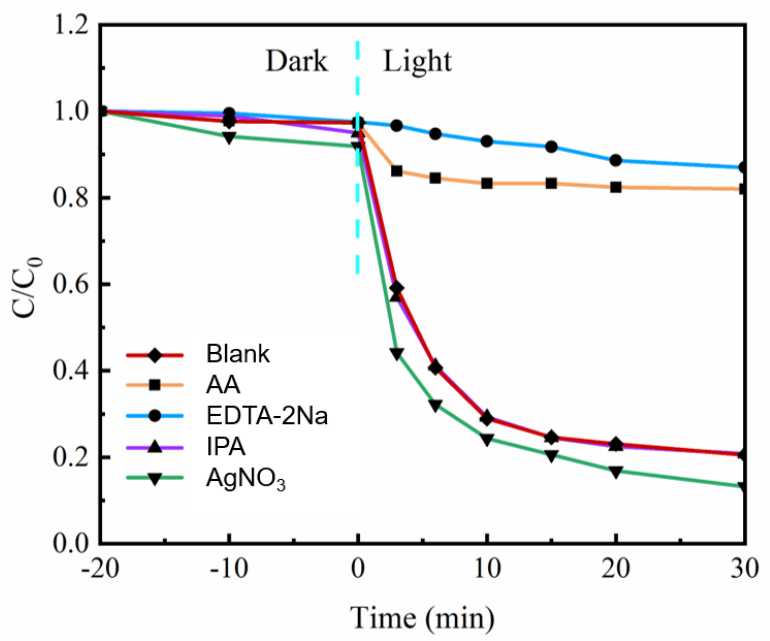

Fig. 7 Radicals trapping experiments in C_3N_4/Ag@AgCl-25 under sunlight irradiation system.

Figure 4's UV-vis absorption spectra show that g-C3N4 has a band gap of 2.87 eV and can absorb visible light with wavelengths as short as 432 nm, at the same time AgCl has a band gap of 2.96 eV and can absorb visible light as short as 419 nm. As a noble metal, Ag not only provides an electron transfer bridge between g-C_3N_4 and AgCl, but also converts the plasma energy of incident photons into surface plasmon resonance effect (SPR) oscillations, which can produce high-energy electrons and hole separation [42] . Because $O_2/\bullet O_2^-$ (-0.33 eV vs. NHE) [43] has a more negative potential than the conduction band potential (CB) of AgCl (-0.06 eV vs. NHE), the reaction of O_2 to $\bullet O_2^-$ is performed in the CB of g-C_3N_4 (-0.91 eV vs. NHE), not at CB of AgCl [37] . The photocatalytic degradation process of g-C_3N_4/Ag@AgCl-25 was as follows: under visible light irradiation, g-C_3N_4 and AgCl valence band (VB) electrons were excited to the corresponding (CB), and Ag produced high-energy electrons due to

SPR effect. Subsequently, the electrons in the CB of AgCl are then transported to the VB of g-C_3N_4 via Ag electron bridge due to the Z-type heterojunction between g-C_3N_4 and AgCl, allowing for the excitation of more g-C_3N_4 electrons to the CB and the transmission of high-energy electrons produced by Ag NPs to the CB of g-C_3N_4. Finally, electrons in the CB of g-C_3N_4 reduce O_2 to strong oxidizing □•O_2^- oxidize TC to CO_2 and H_2O, and holes in the VB of AgCl oxidize TC to CO_2 and H_2O. In this experiment, there are three degradation pathways for TC:

g-C3N4/Ag@AgCl-25 → h^++e^- (2)

e^- + O_2 →□•O_2^- (3)

h^+/□•O_2^- +TC →degraded products (4)

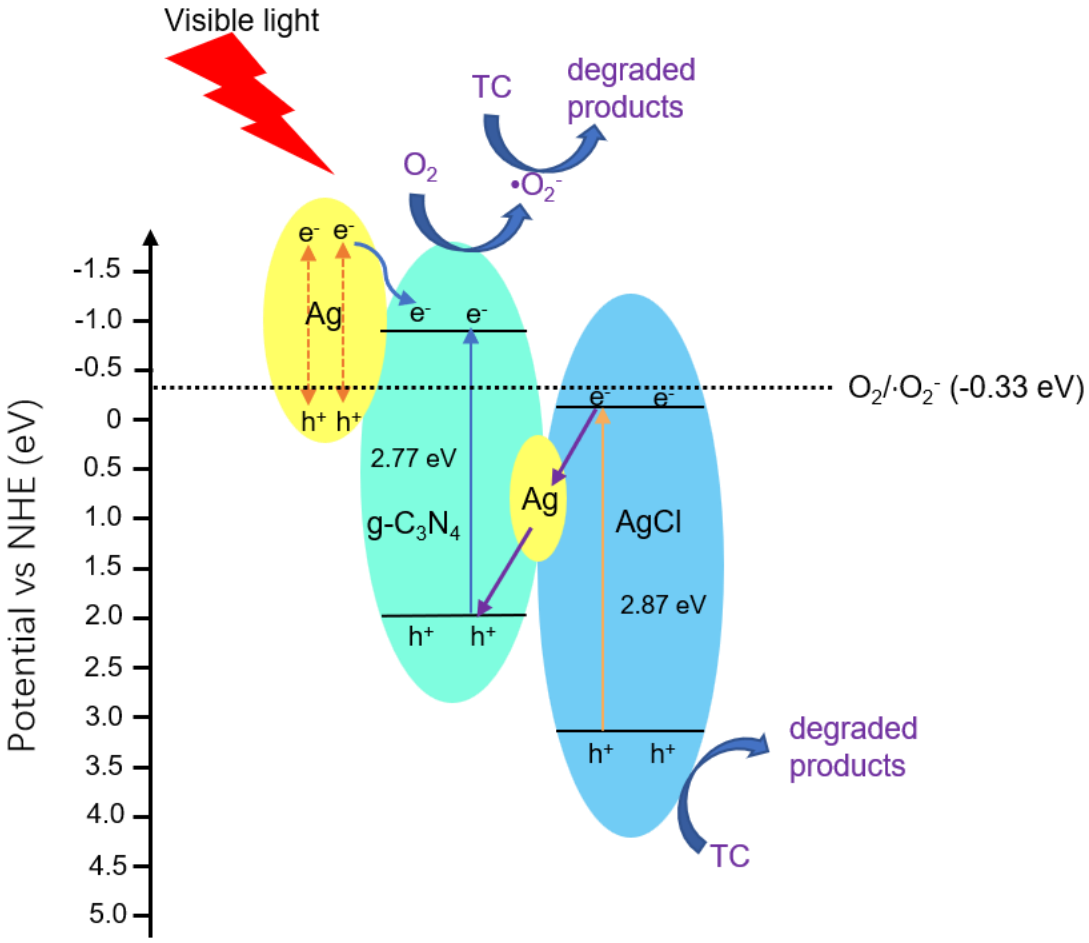

Fig. 8 The mechanism of photocatalytic degradation of TC by g-C_3N_4/Ag@AgCl under visible light.

4. Conclusion

In this paper, a novel Z-type g-C_3N_4/Ag@AgCl heterojunction photocatalyst was successfully obtained, and the photocatalytic performance of the prepared photocatalyst was systematically investigated by oxidation of tetracycline under visible light irradiation. In these samples, the Ag@AgCl loading was 25 wt%, that is, g-C_3N_4/Ag@AgCl-25 showed the highest photocatalytic performance, and the TC degradation efficiency reached 94.9%. The improvement of photocatalytic performance is attributed to the SPR effect of Ag and O-doping, which broadens the absorbance performance of g-C3N4, and the formation of Z-type heterojunctions between AgCl and g-C_3N_4 and Ag as an electron transport bridge promote the transfer of photogenerated electrons between AgCl and g-C_3N_4. In addition, based on the results of the capture experiment, the g-C_3N_4/Ag@AgCl heterostructure follows the typical Z-scheme charge transfer mechanism instead of the traditional type II heterojunction charge transfer mechanism.

Competing Interest Declaration

The authors affirm that they have no known financial or interpersonal conflicts that would have affected the research presented in this paper.

Acknowledgments

Supporters of the research comprise Fund Program for the Scientific Activities of Selected Returned Overseas Professionals in Shanxi Province (20210013), Shanxi Medical University Doctoral Start-up Fund Project (XD2130), Shanxi Provincial Basic Research Program Youth Scientific Research Project (202203021212356) and the Startup Foundation for Doctors of Shanxi Medical University (3C322021041) .

Reference

[1] Q.Q. Zhang, G.G. Ying, C.G. Pan, Y.S. Liu, J.L. Zhao, Comprehensive Evaluation of Antibiotics Emission and Fate in the River Basins of China: Source Analysis, Multimedia Modeling, and Linkage to Bacterial Resistance, Environmental Science & Technology, 49 (2015) 6772-6782.
[2] J.L. Wilkinson, A.B.A. Boxall, D.W. Kolpin, K.M.Y. Leung, R.W.S. Lai, C. Galban-Malagon, A.D. Adell, J. Mondon, M. Metian, R.A. Marchant, A. Bouzas-Monroy, A. Cuni-Sanchez, A. Coors, P. Carriquiriborde, M. Rojo, C. Gordon, M. Cara, M. Moermond, T. Luarte, V. Petrosyan, Y. Perikhanyan, C.S. Mahon, C.J. McGurk, T. Hofmann, T. Kormoker, V. Iniguez, J. Guzman-Otazo, J.L. Tavares, F.G. De Figueiredo, M.T.P. Razzolini, V. Dougnon, G. Gbaguidi, O. Traore, J.M. Blais, L.E. Kimpe, M. Wong, D. Wong, R. Ntchantcho, J. Pizarro, G.G. Ying, C.E. Chen, M. Paez, J. Martinez-Lara, J.P. Otamonga, J. Pote, S.A. Ifo, P. Wilson, N. Udikovic-Kolic, M. Milakovic, D. Fatta-Kassinos, L. Ioannou-Ttofa, J. Vymazal, B.A. Kassa, J. Garric, A. Chaumot, P. Gibba, I. Kunchulia, S. Seidensticker, G. Lyberatos, H.P. Halldorsson, M. Melling, T. Shashidhar, M. Lamba, A. Nastiti, A. Supriatin, N. Pourang, A. Abedini, O. Abdullah, S.S. Gharbia, F. Pilla, B. Chefetz, T. Topaz, K.M. Yao, B. Aubakirova, R. Beisenova, L. Olaka, J.K. Mulu, P. Chatanga, V. Ntuli, N.T. Blama, S. Sherif, A.Z. Aris, L.J. Looi, M. Niang, S.T. Traore, R. Oldenkamp, O. Ogunbanwo, M. Ashfaq, M. Iqbal, Z. Abdeen, A. O'Dea, J.M. Morales-Saldana, H. de la Cruz, I. Navarrete, F. Carvalho, A.B. Gogra, B.M. Koroma, V. Cerkvenik-Flajs, M. Gombac, M. Thwala, K. Choi, H. Kang, J.L.C. Ladu, A. Rico, P. Amerasinghe, A. Sobek, G. Horlitz, A.K. Zenker, A.C. King, J.J. Jiang, R. Kariuki, M. Tumbo, U. Tezel, T.T. Onay, J.B. Lejju, Y. Vystavna, Y. Vergeles, H. Heinzen, A. Perez-Parada, D.B. Sims, M. Figy, D. Good, C. Teta, Pharmaceutical pollution of the world's rivers, Proc. Natl. Acad. Sci. U. S. A., 119 (2022) 10.
[3] A. Fiaz, D.C. Zhu, J.Z. Sun, Environmental fate of tetracycline antibiotics: degradation pathway mechanisms, challenges, and perspectives, Environ. Sci Eur., 33 (2021) 17.
[4] H.Q. Anh, T.P.Q. Le, N. Da Le, X.X. Lu, T.T. Duong, J. Garnier, E. Rochelle-Newall, S.R. Zhang, N.H. Oh, C. Oeurng, C. Ekkawatpanit, T.T. Nguyen, Q.T. Nguyen, T.D. Nguyen, T.N. Nguyen, T.L. Tran, T. Kunisue, R. Tanoue, S. Takahashi, T.B. Minh, H.T. Le, T.N.M. Pham, T.A.H. Nguyen, Antibiotics in surface water of East and Southeast Asian countries: A focused review on contamination status, pollution sources, potential risks, and future perspectives, Sci. Total Environ., 764 (2021) 16.
[5] D.S. Zheng, G.Y. Yin, M. Liu, C. Chen, Y.H. Jiang, L.J. Hou, Y.L. Zheng, A systematic review of antibiotics and antibiotic resistance genes in estuarine and coastal environments, Sci. Total Environ., 777 (2021) 17.
[6] Y.T. Shao, Y.P. Wang, Y.W. Yuan, Y.J. Xie, A systematic review on antibiotics misuse in livestock and aquaculture and regulation implications in China, Sci. Total Environ., 798 (2021) 10.
[7] Y. Li, B. Yu, Z. Hu, H. Wang, Construction of direct Z-scheme SnS2@ZnIn2S4@kaolinite heterostructure photocatalyst for efficient photocatalytic degradation of tetracycline hydrochloride, Chemical Engineering Journal, 429 (2022) 132105.
[8] V. Jayaraman, C. Ayappan, A. Mani, Facile preparation of bismuth vanadate-sheet/carbon nitride rod-like interface photocatalyst for efficient degradation of model organic pollutant under direct sunlight irradiation, Chemosphere, 287 (2022) 132055.
[9] Z. Long, Q. Li, T. Wei, G. Zhang, Z. Ren, Historical development and prospects of photocatalysts for pollutant removal in water, J Hazard Mater, 395 (2020) 122599.
[10] G.Y. Chen, Y. Yu, L. Liang, X.G. Duan, R. Li, X.K. Lu, B.B. Yan, N. Li, S.B. Wang, Remediation of

antibiotic wastewater by coupled photocatalytic and persulfate oxidation system: A critical review, Journal of Hazardous Materials, 408 (2021) 16.
[11] K.N. Qin, Q.L. Zhao, H. Yu, X.H. Xia, J.J. Li, S.F. He, L.L. Wei, T.C. An, A review of bismuth-based photocatalysts for antibiotic degradation: Insight into the photocatalytic degradation performance, pathways and relevant mechanisms, Environ. Res., 199 (2021) 13.
[12] Z.D. Wei, J.Y. Liu, W. Shangguan, A review on photocatalysis in antibiotic wastewater: Pollutant degradation and hydrogen production, Chinese Journal of Catalysis, 41 (2020) 1440-1450.
[13] M.L. Zhang, Y. Yang, X.Q. An, L.A. Hou, A critical review of g-C3N4-based photocatalytic membrane for water purification, Chemical Engineering Journal, 412 (2021) 16.
[14] M.Z. Hussain, Z.X. Yang, Z. Huang, Q.L. Jia, Y.Q. Zhu, Y.D. Xia, Recent Advances in Metal-Organic Frameworks Derived Nanocomposites for Photocatalytic Applications in Energy and Environment, Adv. Sci., 8 (2021) 30.
[15] H. Yang, A short review on heterojunction photocatalysts: Carrier transfer behavior and photocatalytic mechanisms, Mater. Res. Bull., 142 (2021) 9.
[16] Z.J. Wang, B.B. Mei, J.Z. Chen, Removing semiconductor-cocatalyst interfacial electron transfer induced bottleneck for efficient photocatalysis: A case study on Pt/CdS photocatalyst, Journal of Catalysis, 408 (2022) 270-278.
[17] X.W. Zhang, Z. Li, T.F. Liu, M.R. Li, C.B. Zeng, H. Matsumoto, H.X. Han, Water oxidation sites located at the interface of Pt/SrTiO3 for photocatalytic overall water splitting, Chinese Journal of Catalysis, 43 (2022) 2223-2230.
[18] J. Xu, W. Zhong, D. Gao, X. Wang, P. Wang, H. Yu, Phosphorus-enriched platinum diphosphide nanodots as a highly efficient cocatalyst for photocatalytic H2 evolution of CdS, Chemical Engineering Journal, 439 (2022) 135758.
[19] Y.H. Li, Z.R. Tang, Y.J. Xu, Multifunctional graphene-based composite photocatalysts oriented by multifaced roles of graphene in photocatalysis, Chinese Journal of Catalysis, 43 (2022) 708-730.
[20] X.J. Liu, T.Q. Chen, Y.H. Xue, J.C. Fan, S.L. Shen, M. Hossain, M.A. Amin, L.K. Pan, X.T. Xu, Y. Yamauchi, Nanoarchitectonics of MXene/semiconductor heterojunctions toward artificial photosynthesis via photocatalytic CO2 reduction, Coord. Chem. Rev., 459 (2022) 17.
[21] F. Mei, K. Dai, J. Zhang, W. Li, C. Liang, Construction of Ag SPR-promoted step-scheme porous g-C3N4/Ag3VO4 heterojunction for improving photocatalytic activity, Applied Surface Science, 488 (2019) 151-160.
[22] M. Sayed, J.G. Yu, G. Liu, M. Jaroniec, Non-Noble Plasmonic Metal-Based Photocatalysts, Chem. Rev., 122 (2022) 10484-10537.
[23] A. Balakrishnan, M. Chinthala, Comprehensive review on advanced reusability of g-C3N4 based photocatalysts for the removal of organic pollutants, Chemosphere, 297 (2022) 25.
[24] R.T. Guo, J. Wang, Z.X. Bi, X. Chen, X. Hu, W.G. Pan, Recent advances and perspectives of g-C3N4-based materials for photocatalytic dyes degradation, Chemosphere, 295 (2022) 17.
[25] W.F. Kong, Z.P. Xing, B. Fang, Y.Q. Cui, Z.Z. Li, W. Zhou, Plasmon Ag/Na-doped defective graphite carbon nitride/NiFe layered double hydroxides Z-scheme heterojunctions toward optimized photothermal-photocatalytic-Fenton performance, Applied Catalysis B-Environmental, 304 (2022) 12.
[26] G.Z.S. Ling, S.F. Ng, W.J. Ong, Tailor-Engineered 2D Cocatalysts: Harnessing Electron-Hole Redox Center of 2D g-C3N4 Photocatalysts toward Solar-to-Chemical Conversion and Environmental Purification, Advanced Functional Materials, 32 (2022) 33.

[27] S. Ghattavi, A. Nezamzadeh-Ejhieh, A visible light driven AgBr/g-C3N4 photocatalyst composite in methyl orange photodegradation: Focus on photoluminescence, mole ratio, synthesis method of g-C3N4 and scavengers, Compos. Pt. B-Eng., 183 (2020) 16.
[28] W.J. Ong, L.K. Putri, L.L. Tan, S.P. Chai, S.T. Yong, Heterostructured AgX/g-C3N4 (X = Cl and Br) nanocomposites via a sonication-assisted deposition-precipitation approach: Emerging role of halide ions in the synergistic photocatalytic reduction of carbon dioxide, Applied Catalysis B-Environmental, 180 (2016) 530-543.
[29] D. Sun, Y. Zhang, Y.F. Liu, Z.G. Wang, X.C. Chen, Z.Y. Meng, S.F. Kang, Y.Y. Zheng, L.F. Cui, M.L. Chen, M.D. Dong, B. Hu, In-situ homodispersely immobilization of Ag@AgCl on chloridized g-C3N4 nanosheets as an ultrastable plasmonic photocatalyst, Chemical Engineering Journal, 384 (2020) 13.
[30] P. Thakur, P. Raizada, P. Singh, A. Kumar, A.A.P. Khan, A.M. Asiri, Exploring recent advances in silver halides and graphitic carbon nitride-based photocatalyst for energy and environmental applications, Arab. J. Chem., 13 (2020) 8271-8300.
[31] X. Yao, X. Liu, X. Hu, Synthesis of the Ag/AgCl/g-C3N4Composite with High Photocatalytic Activity under Visible Light Irradiation, ChemCatChem, 6 (2014) 3409-3418.
[32] C. Zhang, Z.L. Ouyang, Y. Yang, X. Long, L. Qin, W.J. Wang, Y. Zhou, D.Y. Qin, F.Z. Qin, C. Lai, Molecular engineering of donor-acceptor structured g-C3N4 for superior photocatalytic oxytetracycline degradation, Chemical Engineering Journal, 448 (2022) 11.
[33] X. Yu, J.L. Huang, J.J. Zhao, S.F. Liu, D.D. Xiang, Y.T. Tang, J. Li, Q.H. Guo, X.Q. Ma, J.W. Zhao, Efficient visible light photocatalytic antibiotic elimination performance induced by nanostructured Ag/AgCl@Ti3+-TiO2 mesocrystals, Chemical Engineering Journal, 403 (2021) 12.
[34] J. Yang, W. Fu, C. Chen, W. Chen, W. Huang, R. Yang, Q. Kong, B. Zhang, J. Zhao, C. Chen, Atomic design and fine-tuning of subnanometric Pt catalysts to tame hydrogen generation, ACS Catalysis, 11 (2021) 4146-4156.
[35] K.H. Wu, Y.J. Huang, H.S. Teng, Oligomer-Incorporated Polymeric Layer Framework of Graphitic Carbon Nitride for Effective Photocatalytic Hydrogen Evolution, Part. Part. Syst. Charact., 35 (2018) 8.
[36] H. Zhang, B. Zhang, F. Liang, Y. Fang, H. Wang, A. Chen, Precise regulation of Ultra-thin platinum decorated Gold/Graphite carbon nitride photocatalysts by atomic layer deposition for efficient degradation of Rhodamine B under simulated sunlight, Arab. J. Chem., 15 (2022) 103951.
[37] X. Lin, H. Liu, B. Guo, X. Zhang, Synthesis of AgCl/Ag/AgCl core-shell microstructures with enhanced photocatalytic activity under sunlight irradiation, Journal of Environmental Chemical Engineering, 4 (2016) 4021-4028.
[38] Y. Bao, K. Chen, AgCl/Ag/g-C3N4 Hybrid Composites: Preparation, Visible Light-Driven Photocatalytic Activity and Mechanism, Nanomicro Lett, 8 (2016) 182-192.
[39] L. Jing, M. Xie, Y. Xu, C. Tong, Y. Song, X. Du, H. Zhao, N. Zhong, H. Li, I.D. Gates, J. Hu, O-doped and nitrogen vacancies 3D C3N4 activation of peroxydisulfate for pollutants degradation and transfer hydrogenation of nitrophenols with water, Separation and Purification Technology, 314 (2023) 123540.
[40] W. Chen, J. Huang, Z.C. He, X. Ji, Y.F. Zhang, H.L. Sun, K. Wang, Z.W. Su, Accelerated photocatalytic degradation of tetracycline hydrochloride over CuAl2O4/g-C3N4 p-n heterojunctions under visible light irradiation, Separation and Purification Technology, 277 (2021) 10.

[41] W. Wang, J.J. Fang, S.F. Shao, M. Lai, C.H. Lu, Compact and uniform TiO2@g-C3N4 core-shell quantum heterojunction for photocatalytic degradation of tetracycline antibiotics, Applied Catalysis B-Environmental, 217 (2017) 57-64.
[42] Y. Li, Y. Zhou, W. Zeng, S. Gao, Y. Wu, J. Yang, Acid-Exfoliated g-C3N4 Nanosheets Coated Silver Nanoparticles with Tunable Loading: An Efficient Catalyst for Visible Light Photocatalytic Reaction, ChemistrySelect, 2 (2017) 9947-9952.
[43] X. Li, Y. Qiu, Z. Zhu, H. Zhang, D. Yin, Novel recyclable Z-scheme g-C3N4/carbon nanotubes/Bi25FeO40 heterostructure with enhanced visible-light photocatalytic performance towards tetracycline degradation, Chemical Engineering Journal, 429 (2022) 132130.

Supplementary Files

This is a list of supplementary files associated with this preprint. Click to download.

- Supporting.docx